Poly(catecholamine) coated $CsPbBr_3$ perovskite microlasers: lasing in water and biofunctionalization

Sangyeon Cho[1,2] and Seok Hyun Yun*[1,2]

[1] Wellman Center for Photomedicine, Massachusetts General Hospital and Harvard Medical School, Cambridge, Massachusetts, 02139, USA
[2] Harvard-MIT Health Sciences and Technology, Massachusetts Institute of Technology, Cambridge, Massachusetts, 02139, USA
* Corresponding author: syun@hms.harvard.edu

Keywords: lead halide perovskite, core-shell, waterproof, microlaser, biofunctionalization

Lead halide perovskite (LHP) is a promising material for various optoelectronic applications. Surface coating on particles is a common strategy to improve their functionality and environmental stability, but LHP is not amenable to most coating chemistries because of its intrinsic weakness against polar solvents. Here, we describe a novel method of synthesizing LHP microlasers in a super-saturated polar solvent using sonochemistry and applying various functional coatings on individual microlasers *in situ*. We synthesize cesium lead bromine perovskite ($CsPbBr_3$) microcrystals capped with organic poly-norepinephrine (pNE) layers. The catechol group of pNE coordinates to bromine-deficient lead atoms, forming a defect-passivating and diffusion-blocking shell. The pNE layer enhances the stability of $CsPbBr_3$ in water by 2,000-folds, enabling bright luminescence and lasing from single microcrystals in water. Furthermore, the pNE shell permits biofunctionalization with proteins, small molecules, and lipid bilayers. Luminescence from $CsPbBr_3$ microcrystals is sustained in water over 1 hour and observed in live cells. The functionalization method may enable new applications of LHP laser particles in water-rich environments.

1. Introduction

Lead halide perovskite (LHP), such as $CsPbBr_3$ and $CH_3NH_3PbBr_3$, in the form of micro- and nanocrystals has emerged as an excellent semiconductor material for light-emitting diodes[1,2] and photovoltaic devices[3]. Furthermore, LHP can be used as a gain material for miniature lasers[4–9]. The material gain up to 4,000 cm^{-1} was reported in bulk-like nanocrystals[10]. Lasing from single LHP submicron crystals[8,9] has been demonstrated with threshold pump fluences of 0.2-1 mJ/cm^2. Such miniaturized and efficient LHP lasers may have potential as life-science tools for cell tagging[11], intracellular sensing[12], and deep-tissue imaging[7], if they can be made stable in the aqueous environment and compatible with biological systems. However, thus far this possibility has been out of the question because of the extreme weakness of LHPs in water.

The poor stability of LHPs in water is intimately related to their ionic nature. Unlike traditional inorganic semiconductors that require high-temperature epitaxial growth, LHPs are solution processable at room temperature. This low lattice energy inevitably leads to low stability in the polar environment. Appropriate encapsulation can protect LHP crystals from reactive molecules, enhancing device stability. However, methods to coat LHP, such as atomic layer deposition (ALD)[13,14], calcination[15], Van der Waals force[16], and sol-gel processes[17–19], have been limited to encapsulating ensembles of, not individual, LHP particles in macroscopic hydrophobic matrices. Furthermore, coating precursors used in these methods cause partial damages to LHPs [13,15–18], and the photoluminescence (PL) properties of LHP can be compromised[20].

Herein, we report novel techniques that enable us to add various protective and functional materials on the surface of inorganic LHP microlasers. We use organic poly-norepinephrine (pNE) for an initial coating on $CsPbBr_3$ microcrystals. The pNE polymer layer then allows us to conjugate various biological functional materials via spontaneous reactions at room temperature. We demonstrate core-shell LHP microparticles with 2-fold improved quantum-

yield and 2,000-fold improved material stability in water. Functionalized LHP particles internalized by biological cells generate bright luminescence in the cytoplasm.

2. Results

2.1. One-pot synthesis of pNE-coated $CsPbBr_3$ microlasers

Figure 1a depicts the schematic of our novel core-shell particle synthesis based on sonochemical crystallization of the LHP core and subsequent polymerization of the pNE shell. First, CsBr (75 mM) and $PbBr_2$ salts (75 mM) are added into N,N-dimethylformamide (DMF) in room temperature. The $PbBr_2$ salts are partially dissolved in the DMF solution to produce Pb^{2+} and Br^- and the complexation[21] of $PbBr_3^-$ and $PbBr_4^{2-}$. These ions react with undissolved CsBr salts and form a thin layer of orange-color $CsPbBr_3$ on their surface via fast interfacial reactions (Figure S1a). Ultrasonication is applied to the mixture for about two minutes using a bath- or tip-based ultrasonicator (Figure S1b). Once ultrasonication starts, the remaining salts with interfacial $CsPbBr_3$ are broken into smaller pieces by ultrasonic forces and completely dissolved within 30-50 seconds. As the $PbBr_4^{2-}$ concentration reaches a critical level over saturation, the nuclei of $CsPbBr_3$ are spontaneously formed at the vicinity of ultrasonic bubbles and grow to micro- and submicron crystals via: $Cs^+(sol) + PbBr_4^{2-}(sol) \rightarrow CsPbBr_3(s) + Br^-(sol)$. The growth of microcrystals ceases after about 2 minutes of ultrasonication (Figure S1b).

This one-pot synthesis is two-order-of-magnitude faster than the previous surface-initiated growth process[22] that required ~ 20 hours to grow crystals to the size of a few μm. Scanning electron microscopy (SEM) of the $CsPbBr_3$ microcrystals showed cuboidal shapes without any noticeable cracked edges (Figure S1c and d). The addition of a nonionic surfactant, such as polysorbate 80, to the precursor solution resulted in an anisotropic growth of microplates and nanowires without perturbing supersaturation (Figure S1e).

Once the growth of $CsPbBr_3$ microcrystals is completed, they remain stable under the dynamic equilibrium in the saturated DMF solution. This opens up the opportunity to coat the

surface by adding catecholamines. Poly-catecholamine coating, as found in mussel's sticky footage containing dihydroxyphenylalanine (DOPA) and tyrosine, is known for its ability to coat a wide range of materials[23,24]. Following the sonochemical synthesis, we added 4 mg/mL of a norepinephrine (NE) bitartrate salt and a pallet of sodium hydroxide (NaOH) into the solution (Figure 1a). After incubating at 50 °C for 1 hour, pNE shells appear on the surface of the individual microcubes and microplates in the solution (Figure 1b). The solution maintains green fluorescence under ultra-violet (UV) light. It is possible to scale up the production of pNE-coated $CsPbBr_3$ particles simply by increasing the volume of the reactants (Figure 1c). Typically, we obtained about 10^7 microcrystals per ml of DMF.

Energy-dispersive density spectroscopy (EDS), X-ray photoluminescence spectroscopy (XPS), and powder x-ray diffraction (PXRD) confirmed that the lattice sizes and stoichiometry of $CsPbBr_3$ after the coating were unchanged. The XPS clearly shows the presence of the pNE shell (Figures 1d). The nitrogen-to-oxygen signal ratio (N/O) was measured to be ~ 0.4, close to the 0.33 ratio of the NE (Figure 1e). PXRD reveals the orthorhombic structure of single-crystalline $CsPbBr_3$ (space group *Pbnm*, A=8.20 Å, B=8.24 Å, C=11.74 Å) (Figure 1f). Fourier-transform infrared (FTIR) spectroscopy showed absorption peaks at 3000-3500 cm^{-1} corresponding to the amine and hydroxyl groups (Figure 1g). The characteristics absorbance peaks of the catechol and indole ring appeared at 1514 cm^{-1} (Figure 1g). These functional groups offer binding sites to conjugate biomaterials via Schiff-base reactions and Michael additions.

2.2. Structural and optical characterization

SEM and TEM images taken at different reaction times provided further insights into the coating process (**Figure 2**a). After 15 min of polymerization, a 25-60 nm thick, conformal shell appears unevenly on the surface. This morphology is consistent with our expectation that the NE molecules polymerize laterally via oxidative covalent linkage and grow vertically via π-π

staking and Pb^{2+}-assisted coordination[24]. Initially, the thickness of the conformal pNE shell increases linearly with incubation time, but after 30 min it saturates at 40-80 nm depending on the crystallization direction (Figures 2b and 2c). The growth kinetics was analyzed using the sigmoidal equation[25]. In the [010] direction, the maximum growth rate was 4.4 nm/min and the thickness of the pNE layer after 30 min was 76 nm. In the [100] direction, the maximum growth rate was 2 nm/min, and the thickness was 41 nm. This asymmetry is attributed to the smaller steric hindrance at the regular octahedral site of the (010) surface compared to the tilted octahedral site of the (110) surface (Figure 2c, inset).

When the polymerization time exceeds 30 min, mesoporous pNE sheets appear outside the conformal pNE shell. SEM and TEM images present that the mesoporous pNE shell consists of multiple sheets grown along the surface normal (Figure 2a). Each sheet is 1 to 2 μm in lateral size and contains numerous nanopores with 20 to 50 nm sizes and pNE aggregates with 3 to 8 nm in diameter (Figure S3). We speculate that these colloidal pNE aggregates are stacked over time forming the supramolecular sheet structure. The mesoporous pNE shell in saturated DMF solution appears transparent. However, when the saturated DMF was dried out, the mesoporous pNE became dark (light-absorbing) (Figure 2d). Re-soaking the particles into saturated DMF solution recovers the transparency of the pNE shell. This reversible effect is due to the swelling property of the mesoporous pNE. DMF molecules intercalated into the pNE layers disrupt the pi-pi or cation-pi interactions and affect optical absorption[26] and average refractive index[27] of the pNE organogel.

High-resolution XPS showed that only 4*f* orbital electrons in the Pb atoms underwent a spectral blue-shift of 0.8 eV and also a broadening of 0.2 eV after coating (Figure 2e and Figure S3). This indicates that the electronegative catechol group with lone pair electrons binds to the electropositive under-coordinated Pb atoms, forming Lewis acid-base adducts. A density functional theory (DFT) simulation suggests that two oxygen atoms in the catechol form a bidentate binuclear surface complex with the under-coordinated Pb atoms in the (010) surface

(Figure 2f), as found in other catechol-metal oxides[28]. The binding energy of pNE to the (010) surface (Figure S4a) was calculated to be –0.13 eV, indicating that this process is thermodynamically flavored. The DFT calculation of density of states suggests that the Lewis acid-base adduct can remove shallow trap states between the band edges (Figure S4b).

To confirm this passivation effect, we measured photoluminescence (PL). After conformal pNE coating, the absolute PL quantum yield (η) of $CsPbBr_3$ microparticles increased from 1.5 to 2.9%, and the PL emission peak wavelength was blue-shifted from 531 to 525 nm (Figure S4c). These changes indicate reduced shallow-trap density by surface defect passivation[29]. Under cyclic continuous-wave optical excitation, the PL intensity of uncoated $CsPbBr_3$ showed hysteresis due to the filling and saturation of carrier trap states[30]. The hysteresis was nearly eliminated after coating (Figure 2g). The measured transient PL decay curves (Figure 2h) were fitted to a double-exponential model (Table S1) with two lifetime constants, τ_1 and τ_2, accounting for fast carrier quenching through trap states and slow radiative recombination, respectively[31]. Coated $CsPbBr_3$ particles exhibited τ_1 of 2 ns and τ_2 of 12.2 ns, about 2-fold increase compared to uncoated $CsPbBr_3$ with τ_1 of 1.3 ns and τ_2 of 6.2 ns. Cyclic voltammetry (Figure S5) further confirmed the passivation effect of pNE.

2.3. Enhanced material stability and lasing in water

Material stability against water was dramatically improved after pNE coating (**Figure 3**a). When immersed in water, uncoated $CsPbBr_3$ microparticles dissolve immediately (< 0.3 s). By contrast, coated $CsPbBr_3$ microparticles maintained optical absorbance and green fluorescence in water for ~ 10 min. This 2,000-fold enhanced material stability enabled us to observe lasing from single core-shell microparticles in water upon optical pumping (480 nm, pulse width: 5 ns) (Figure 3b and S6). The far-field emission pattern of a core-shell $CsPbBr_3$ particle with a size of 4 μm showed uniform fluorescence below lasing threshold and bright scattering spots above threshold (Figure 3c; see Figure S7 for a 1.5-μm-sized particle and S7b for a 6-μm-sized

particle). A narrowband lasing peak at 537 nm is evident, superimposed on a broad fluorescence background (Figure 3d). This laser particle showed a light-in-light-out (L-L) curve with a pump threshold of 0.85 mJ/cm^2, 3.4 folds higher than the threshold fluence in the air (n=1) due to the higher refractive index (n=1.33) of the water (Figure S7c). The linewidth narrowing near the threshold is another evidence of lasing (Figure 3e). The narrowest linewidth near the threshold was about 0.5 nm in FWHM. Lasing in water lasted over about 100 pump pulses at a fluence of 1 mJ/cm^2, after which lasing ceased due to the photodegradation of $CsPbBr_3$.

We measured a large number of $CsPbBr_3$ particles in the ambient air and found that the pNE coating allowed substantially smaller $CsPbBr_3$ microcrystals to reach lasing threshold, compared to uncoated $CsPbBr_3$ particles (Figure S8). Furthermore, the pulse-to-pulse intensity variation from the core-shell particles was 6 times smaller than uncoated particles (Figure S8). These enhanced lasing characteristics are due to the defect passivation by pNE coating.

2.4. Biofunctionalization

The considerable lifetime (>5 min) of core-shell laser particles in water allow many spontaneous chemical reactions to be used for surface functionalization. We performed four different proof-of-concept experiments to demonstrate functionalization with biomolecules.

First, we encapsulated core-shell perovskite particles with lipid bilayers (**Figure 4**a). For this, we prepared 1-μm-size large unilamellar vesicles (LUVs) made of DIR dye-labeled, 1,2-dioleoyl-sn-glycero-3-phosphoethanolamine (DOPE) and 1,2-dioleoyl-3-trimethylammonium-propane (DOTAP) using a conventional extrusion method[32]. When mixed with pNE-coated particles in water, LUVs are deposited on the surface of the pNE via direct vesicle fusion (Figure 4b, inset). The lipid bilayer-functionalized core-shell $CsPbBr_3$ microparticles produced PL for over 1 hour in water (Figure 4b). Further improved stability enabled us to deliver the lipid-coated particles to the cytoplasm of 4T1 breast cancer cells *in*

vitro (Figure 4c). Upon excitation, distinct green fluorescence is generated from the particles in the cytoplasm.

Secondly, we conjugated biotin-dPEG$_{23}$-NH$_2$ to the pNE shell using Schiff-base reaction (Figure 4d). The biotinylated LHP particles are firmly anchored on a streptavidin-coated plate (Figure 4e). Under a strong pump fluence (2 mJ/cm^2), the optical radiation force moves non-biotinylated particles[33], but biotinylated particles remain stationary (Figure 4f).

Thirdly, we functionalized core-shell LHP particles with fluorescent proteins (Figure 4g). DsRed fluorescent proteins (RFPs) in the phosphate buffered saline (PBS) were mixed with pNE-coated $CsPbBr_3$ particles in ethanol with 1:1 volume ratio. The mixture was incubated for 5 min for the RFPs to attach to the pNE via Schiff-base reaction. Fluorescence spectroscopy (Figure 4h) and imaging (Figure 4i) confirmed the presence of RFP on the surface of the microparticles. The gradual binding of RFP is evident in the spectral shift of the laser peak and the increase of RFP emission (Figures 4j and S9). It is noteworthy that partial anion exchange chemistry can tune the fluorescence color of LHP particles via solid-state halide diffusion[34]. The LHP-protein hybrid microparticles have potential for biological applications such as multiplexed assay[35], single molecule biophysics[36] and hyperspectral imaging[37].

Lastly, we attached bioluminescent Renilla luciferase-8 (Rluc8) on the surface of particles (Figure 4k). Rluc8-coated hybrid particles (a mean size of 4 μm) on a glass substrate produce bioluminescence centered at 420 nm (Figure 4l) when 10 μl PBS solution of 50 μM of C6-methoxyphenylcoelenterazine (MeO-CTZ) was applied. When excited with continuous-wave laser at 491 nm, the hybrid particles showed bright green fluorescence of $CsPbBr_3$ (Figure 4l).

It is possible to attach a variety of other functional materials, such as alkanethiol molecules for hydrophobic functionalization in organic solvents (Figure S10), plasmonic nanoparticles for local-field enhancement, and conductive polymers for charge-transfer coupled redox sensor to pNE coated microparticles. As alternatives to polycatechol, self-polymerizable

polyethyleneimine[38] with multiple nitrogen atoms and polyphenol coating[39] may be used for the coating of LHP particles.

3. Conclusion

In summary, we have demonstrated facile sonochemical crystallization, pNE coating, and large-scale synthesis of single core-shell-type $CsPbBr_3$ microlasers. The pNE shell passive surface defects to enhanced luminescence and extended the lifetime of $CsPbBr_3$ microparticles in water from sub-second to several minutes. We demonstrated stable lasing from core-shell $CsPbBr_3$ microparticles in water. Also, the organic polymer provides rich chemical groups to attach various biomaterials. Biofunctionalization of LHP microlasers opens new possibilities for biological applications.

4. Experimental Section

Materials and reagents. CsBr (99.99%), $PbBr_2$ (99.99%), NaOH (Pallets), (±)-Norepinephrine (+)-bitartrate salt, N,N-Dimethylformamide (anhydrous, 99.8%), Ethanol (anhydrous, ≥99.5%) were purchased from Sigma-Aldrich. 1,2-dioleoyl-sn-glycero-3-phosphoethanolamine (DOPE) and 1,2-dioleoyl-3-trimethylammonium-propane (DOTAP) were purchased from Avanti polar lipid. $DiIC_{18}(7)$ (1,1'-Dioctadecyl-3,3,3',3'-Tetramethylindotricarbocyanine Iodide) dye (DIR), proLong gold antifade mountant with DAPI, and streptavidin-coated 96 well plates were purchased from Thermo-Scientific. Biotin-$dPEG_{23}$-NH_2 were purchased from Quanta Biodesign. Phosphate Buffered Saline (PBS, pH=7.4) was purchased from Invitrogen/Gibco. rDSRed-express protein was purchased from Takara Bio. MeO-eCTZ was purchase from Nanolight and RLuc8 (in PBS, pH 7.4) was purchased G-Biosciences. All reagents were used as received without further purification.

Synthesis of core-shell $CsPbBr_3$-pNE microcrystals. Sonochemical synthesis of core $CsPbBr_3$ microcrsytals. CsBr and $PbBr_2$ were dispersed at an equal concentration in 1 mL of

N,N-dimethylformamide (DMF) in a vial. The typical concentration of the precursor salts was 0.075 M each. The vial was then placed into a bath-type ultrasonicator (Elmasonic P60H, Elma) or a single step tip ultrasonicator (Fisherbrand Q125) in room temperature and irradiated with ultrasonic waves at frequency of 20-80 kHz. After 2-3 min of ultrasonication, single-phase $CsPbBr_3$ microcrystals were spontaneously crystallized and colloidally dispersed in the solution. Sonochemically synthesized LHPs microparticles stay stable in DMF due to supersaturation and can undergo pNE coating. 4 mg of (±)-Norepinephrine (+)-bitartrate salt and a pallet of NaOH were mixed with the solution and vortexed for 3 s. Undissolved NaOH pallet was discarded. The vial with untightened cap was shaken at 800 rpm in 50 °C for 20~30 min to construct conformal pNE coating, and for 1 h to form mesoporous pNE coating. The product was centrifuged at 4000 rpm for 2 min and washed several times with ethanol the remaining precursors. Finally, the core-shell particles were stored in ethanol for further use.

Biofunctionalization. For perovskite-lipid-bilayer hybrid, first, the large unilamellar vesicles (LUVs) consisting of DOPE and DOTAP was synthesized by using conventional extrusion method[1]. Prepared LUVs in water were stained with DIR dye for near-infrared fluorescence imaging. For lipid-bilayer coating, the LUVs were mixed with pNE-coated $CsPbBr_3$ particles in ethanol in a 1:1 vol/vol ratio and then vortexed for 1 minute for sufficient encapsulations. For cell experiments, the lipid-coated particles were added to living 4T1 breast cancer cells and the cells were incubated at 37 °C and 5% CO_2 for 10 minutes. After delivering process, cells were stained after fixation with DAPI for nucleus and imaged under the fluorescence and bright-field microscopy to confirm particle uptake (Keyence BZ-X700 microscope). For biotinylated perovskite particles, pNE-coated $CsPbBr_3$ in ethanol was mixed with 6 mg of biotin-$dPEG_{23}$-NH_2 and then incubated at room-temperature for 1 hour. After the biotinylation, the product was washed two times with ethanol. For tethering experiments, the prepared particles were drop-casted to the streptavidin-coated 96 well plate and dry-out the ethanol solvent using N_2 flows. For perovskite-RFP hybrid, pNE-coated $CsPbBr_3$ was mixed

in PBS buffer containing rDSRed-express protein (100 μg/1 mL). After incubation for 5 min, the product was centrifuged at 8000 rpm for 5 min and then the supernatant was removed. The product was washed two times with fresh PBS to remove unattached proteins. The perovskite-RFP hybrid was re-dispersed in fresh PBS buffer and immediately transferred to a glass substrate for optical characterization. For perovskite-Rluc hybrid, pNE-coated $CsPbBr_3$ was mixed in PBS buffer containing Rluc8 protein (5 mg/1 mL). After incubation for 5 min, the product was centrifuged at 8000 rpm for 5 min and then the supernatant was removed. The product was washed two times with fresh PBS to remove unattached proteins. The final product was drop-casted on the glass substrate. For generating bioluminescence, MeO-CTZ (50 μM in PBS buffer) was mixed with the product solution on the substrate.

Material characterization. For SEM and EDX measurements, samples were transferred onto a chipped Si wafer by drop casting and imaged using a Zeiss Merlin High-resolution SEM equipped with an EDX detector operated at 15 kV. For TEM measurements, samples were prepared by drop casting microparticles onto TEM grids (Ted Pella). TEM images were acquired using a FEI Tecnai Multipurpose TEM operated at 120 kV. The illumination beam was expanded to avoid sample damage. For power x-ray diffraction (PXRD) measurements, PXRD patterns over 2θ angles from 10° to 60° were collected using a PANalytical X'Pert PRO high-resolution X-ray diffraction system with a CuKα irradiation source. These measurements were performed at the MIT Center for Material Science and Engineering (CMSE). For AFM measurements, sample images were acquired with a Nanoscope IV Scanning Probe Microscope (Veeco Metrology Group) operating in a tapping mode. For XPS measurements, the spectrum was collected using a physical Electronics Versaprobe II with monochromated Al (1486.6 eV) irradiation source having a beam size of 200 μm. The survey analysis was conducted with step sizes of 0.8 eV and a digital pass energy of 182.8 eV. The high energy resolution scan of the Cs3d, Pb4f, Br3p, C1s, O1s regions was taken with step sizes of 0.1 eV and the digital pass energy of 23.5 eV. For FTIR spectroscopy measurements, the reflection spectrum from the

sample on a chipped Si wafer were measured using a Thermo Fisher 6700 FTIR Bench. These measurements were performed at the MIT center for material science and engineering (CMSE).

Optical characterization. Optical absorbance spectra were measured using a spectrophotometer (BioTEk, Epoch2). Widefield brightfield and fluorescence images were obtained using an optical microscope (Keyence, BZ-X). For time-resolved photoluminescence measurements, we used a picosecond laser (VisIR-765, PicoQuant), which was frequency-doubled to 382 nm using a nonlinear BBO crystal (Fig. S20), a single-photon avalanche photodiode (Micro Photonics Devices) with a response time of 50 ps, and a time-correlated single-photon counting board (TimeHarp 260, PicoQuant) with a resolution of 25 ps. For absolute quantum yield measurements, a vial of colloidally dispersed LHPs microcrystals in solution was placed in an integrating sphere (Thorlabs) and excited using the 382-nm frequency-doubled picosecond laser. The spectra of light collected from the integrating sphere was coupled, via a multimode fiber, to a spectrometer (Shamrock, Andor) consisting of a diffraction grating and an electron multiplier charge-coupled device (EMCCD) camera. For lasing experiments in water, LHPs microcrystals were centrifuged at 8000 rpm for 2 minutes and removed the supernatant. The particles were mixed with pure water and vortexed for 30 seconds for uniform dispersion. The particle solution was transferred onto a standard 35 mm glass-bottom dish. The specimen was placed in a home-built epi-fluorescence microscopy setup (Supplementary Fig. 13). The pump source was an optical parametric oscillator (OPO, Optotek HE 355 LD) tuned to 480 nm and circularly polarized, with a repetition rate of 20 kHz and a pulse duration of 4 ns. Using a 0.6 NA, 50x air objective lens (Nikon), the full-width-at-half-maxima (FWHM) size of the pump beam on the sample was adjusted to ~38 μm. The emission from the sample collected by the objective lens was passed through a dichroic mirror and a dichroic filter and split to an EMCCD camera (Luca, Andor) for wide-field imaging and to the grating-based EMCCD spectrometer (Shamrock, Andor). For the experiment for lasing LHP particles in water, we used 0.6 NA, 50x air objective lens (Nikon). With an entrance slit width

of 20 μm, the measurement spectral resolution was ~0.13 nm. For real-time observation of RFP attachment, the 10 μL of 5 nm pNE-coated perovskite particles in ethanol were transferred onto a standard 35 mm glass-bottom dish and dried out the ethanol using N_2 flow. Then additional 3 mL of ethanol was added to the dish. Under nanoseconds optical pumping at 20 Hz and single-shot acquisition using external triggering, the spectra was recorded during the addition of 1 μL of RFP solution on the top of the surface of the ethanol solution in the dish. As an excitation source for photoluminescence analysis, we used a continuous-wave, diode-pumped laser (491 nm, Cobolt Calypso). All measurements were conducted at room temperature.

Density functional theory (DFT) calculation. First principle calculations were carried out using the quantum espresso package, a density functional theory (DFT) approach. The electron-ion interactions described by a Standard-Solid-State-Pseudopotentials (SSSP) with electrons from Cs 6s, 5p, 5d; Pb 6s, 6p, 5d; Br 4s 4p; C, N and O 2s, 2p; H 1s shells included in the calculations. The Perdew–Burke–Ernzerhof (PBE) version of the generalized gradient approximation (GGA) were adopted for exchange correlation. The energy cutoff of 30 and 180 Rydberg was adopted for wavefunctions and charge density expansion, respectively. The k-point mesh 3x3x1 were used for orthorhombic $CsPbBr_3$ unit cell and surface structure calculations, respectively. Surface slabs were modelled as $PbBr_2$-terminated slabs, which has 9 layers of CsBr and $PbBr_2$ in total. 15 Å vacuum was added on top of the slab surface to minimize the interaction between the adjacent slabs. In all electronic structure calculations, the self-consistent field (SCF) was terminated when the estimated energy error was $< 10^{-4}$ Rydberg. All crystal structures were relaxed to their lowest energy structures using Broyden-Fletcher-Goldfarb-Shanno minimization (BFGS).

Electrochemical bandgap characterization. Fluorine doped tin oxide (FTO) substrates were rinsed with DI water and acetone and dried out in prior to use. LHPs microparticles were transferred onto fluorine doped tin oxide (FTO) glass electrodes by drop-casting. Dichloromethane (DCM) was used as the solvent. The conducting electrolytes were 0.1M of

tetrabutylammonium tetrafluoroborate ($TBABF_4$). The FTO/perovskite electrodes functioned as the working electrode, a Pt mesh (1 cm^2) as the counterelectrode, and homemade Ag/AgCl wire (a Ag wire having AgCl deposited on its surface) as the pseudoreference electrode. We carried out cyclic voltammetry (CV) measurements using a Biologic VSP 16-channel potentiostat and a three-electrode electrochemical cell with a porous glass frit separating the counter electrode from the working and reference electrodes. The thermodynamic potential of the electrodes was measured dissolving an amount of ferrocene into the solution.

Finite-Difference Time-Domain (FDTD) simulation. FDTD simulations for 850 nm perovskite core-shell resonators (core material: $CsPbBr_3$ (n=2.5), core dimension: 750 nm x 750 nm x 600 nm, shell material: pNE (n=1.51), shell thickness: 50 nm) on a glass substrate in air were performed using commercial software (Lumerical). The extremely fine mesh was set around the cube (Free-triangular, size 5 nm). The time apodization was centered at 450 fs with time width of 100 fs.

Acknowledgements

The authors thank Dr. Hao Yan for cell experiment and Dr. Soyoung Kim and Prof. Surendranath at MIT for helping electrochemical characterizations. This research was supported in part by the Massachusetts General Hospital Research Scholar Award and National Institutes of Health (grant no. DP1EB024242). S.C. acknowledges the Samsung Scholarship. Part of this work used the facilities in the Center for Materials Science and Engineering at MIT.

References

[1] H. Cho, S.-H. Jeong, M.-H. Park, Y.-H. Kim, C. Wolf, C.-L. Lee, J. H. Heo, A. Sadhanala, N. Myoung, S. Yoo, *Science* **2015**, *350*, 1222.

[2] Y. Cao, N. Wang, H. Tian, J. Guo, Y. Wei, H. Chen, Y. Miao, W. Zou, K. Pan, Y. He, *Nature* **2018**, *562*, 249.

[3] M. A. Green, A. Ho-Baillie, H. J. Snaith, *Nat. Photonics* **2014**, *8*, 506.

[4] G. Xing, N. Mathews, S. S. Lim, N. Yantara, X. Liu, D. Sabba, M. Grätzel, S. Mhaisalkar, T. C. Sum, *Nat. Mater.* **2014**, *13*, 476.

[5] Y. Jia, R. A. Kerner, A. J. Grede, B. P. Rand, N. C. Giebink, *Nat. Photonics* **2017**, *11*, 784.

[6] H. Zhu, Y. Fu, F. Meng, X. Wu, Z. Gong, Q. Ding, M. V Gustafsson, M. T. Trinh, S. Jin, X. Y. Zhu, *Nat. Mater.* **2015**, *14*, 636.

[7] S. Cho, M. Humar, N. Martino, S. H. Yun, *Phys. Rev. Lett.* **2016**, *117*, 193902.

[8] E. Tiguntseva, K. Koshelev, A. Furasova, P. Tonkaev, V. Mikhailovskii, E. V Ushakova, D. G. Baranov, T. Shegai, A. A. Zakhidov, Y. Kivshar, *ACS Nano* **2020**, *14*, 8149.

[9] S. Cho, Y. Yang, M. Soljačić, S. H. Yun, *arXiv Prepr. arXiv2007.09265* **2020**.

[10] P. Geiregat, J. Maes, K. Chen, E. Drijvers, J. De Roo, J. M. Hodgkiss, Z. Hens, *ACS Nano* **2018**, *12*, 10178.

[11] N. Martino, S. J. J. Kwok, A. C. Liapis, S. Forward, H. Jang, H.-M. Kim, S. J. Wu, J. Wu, P. H. Dannenberg, S.-J. Jang, Y.-H. Lee, S.-H. Yun, *Nat. Photonics* **2019**, *13*, 720.

[12] M. Schubert, L. Woolfson, I. R. M. Barnard, A. M. Dorward, B. Casement, A. Morton, G. B. Robertson, P. L. Appleton, G. B. Miles, C. S. Tucker, *Nat. Photonics* **2020**, *14*, 452.

[13] A. Loiudice, S. Saris, E. Oveisi, D. T. L. Alexander, R. Buonsanti, *Angew. Chemie Int. Ed.* **2017**, *56*, 10696.

[14] H. Yu, X. Xu, H. Liu, Y. Wan, X. Cheng, J. Chen, Y. Ye, L. Dai, *ACS Nano* **2019**, *14*, 552.

[15] Z. Li, E. Hofman, J. Li, A. H. Davis, C. Tung, L. Wu, W. Zheng, *Adv. Funct. Mater.* **2018**, *28*, 1704288.

[16] H. Wu, S. Wang, F. Cao, J. Zhou, Q. Wu, H. Wang, X. Li, L. Yin, X. Yang, *Chem. Mater.* **2019**, *31*, 1936.

[17] H. Huang, B. Chen, Z. Wang, T. F. Hung, A. S. Susha, H. Zhong, A. L. Rogach, *Chem. Sci.* **2016**, *7*, 5699.

[18] S. Huang, Z. Li, L. Kong, N. Zhu, A. Shan, L. Li, *J. Am. Chem. Soc.* **2016**, *138*, 5749.

[19] S. Li, D. Lei, W. Ren, X. Guo, S. Wu, Y. Zhu, A. L. Rogach, M. Chhowalla, A. K.-Y. Jen, *Nat. Commun.* **2020**, *11*, 1.

[20] N. Erathodiyil, J. Y. Ying, *Acc. Chem. Res.* **2011**, *44*, 925.

[21] S. J. Yoon, K. G. Stamplecoskie, P. V Kamat, *J. Phys. Chem. Lett.* **2016**, *7*, 1368.

[22] Y. Fu, F. Meng, M. B. Rowley, B. J. Thompson, M. J. Shearer, D. Ma, R. J. Hamers, J. C. Wright, S. Jin, *J. Am. Chem. Soc.* **2015**, *137*, 5810.

[23] H. Lee, S. M. Dellatore, W. M. Miller, P. B. Messersmith, *Science* **2007**, *318*, 426.

[24] S. Hong, J. Kim, Y. S. Na, J. Park, S. Kim, K. Singha, G. Im, D. Han, W. J. Kim, H. Lee, *Angew. Chemie Int. Ed.* **2013**, *52*, 9187.

[25] S. I. A. Cohen, M. Vendruscolo, M. E. Welland, C. M. Dobson, E. M. Terentjev, T. P. J. Knowles, *J. Chem. Phys.* **2011**, *135*, 1.

[26] M. D'Ischia, A. Napolitano, A. Pezzella, P. Meredith, T. Sarna, *Angew. Chemie - Int. Ed.* **2009**, *48*, 3914.

[27] G. Loget, J. B. Wood, K. Cho, A. R. Halpern, R. M. Corn, *Anal. Chem.* **2013**, *85*, 9991.

[28] Y. Liu, K. Ai, L. Lu, *Chem. Rev.* **2014**, *114*, 5057.

[29] S. M. Vorpahl, S. D. Stranks, H. Nagaoka, G. E. Eperon, M. E. Ziffer, H. J. Snaith, D. S. Ginger, *Science* **2015**, *348*, 683.

[30] Y. Shao, Z. Xiao, C. Bi, Y. Yuan, J. Huang, *Nat. Commun.* **2014**, *5*, 5784.

[31] H. Zhang, Y. Wu, C. Shen, E. Li, C. Yan, W. Zhang, H. Tian, L. Han, W. Zhu, *Adv. Energy Mater.* **2019**, *9*, 1803573.

[32] L. A. Morton, J. P. Saludes, H. Yin, *JoVE* **2012**, e4151.

[33] M. Liu, T. Zentgraf, Y. Liu, G. Bartal, X. Zhang, *Nat. Nanotechnol.* **2010**, *5*, 570.

[34] L. Dou, M. Lai, C. S. Kley, Y. Yang, C. G. Bischak, D. Zhang, S. W. Eaton, N. S. Ginsberg, P. Yang, *Proc. Natl. Acad. Sci.* **2017**, *114*, 7216.

[35] S. F. Kingsmore, *Nat. Rev. Drug Discov.* **2006**, *5*, 310.

[36] T. Ha, P. Tinnefeld, *Annu. Rev. Phys. Chem.* **2012**, *63*.

[37] S. J. J. Kwok, N. Martino, P. H. Dannenberg, S.-H. Yun, *Light Sci. Appl.* **2019**, *8*, 1.

[38] T. Xia, M. Kovochich, M. Liong, H. Meng, S. Kabehie, S. George, J. I. Zink, A. E. Nel, *ACS Nano* **2009**, *3*, 3273.

[39] T. S. Sileika, D. G. Barrett, R. Zhang, K. H. A. Lau, P. B. Messersmith, *Angew. Chemie Int. Ed.* **2013**, *52*, 10766.

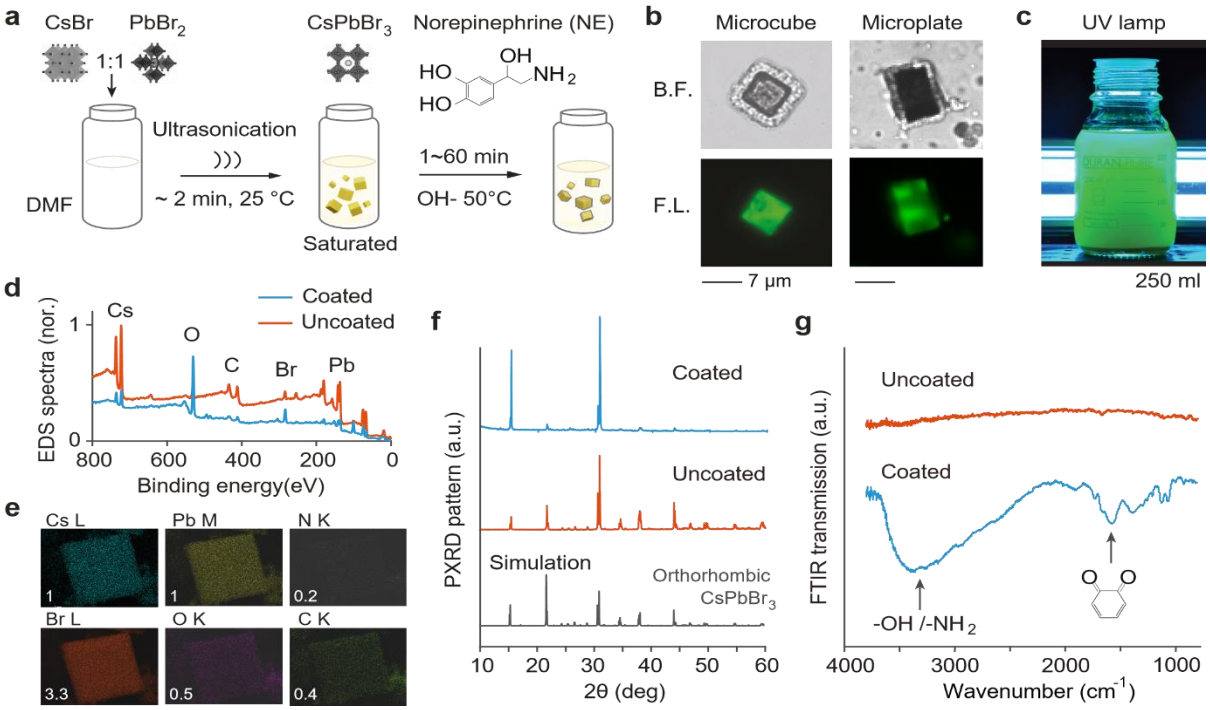

Figure 1. One-pot synthesis of core-shell $CsPbBr_3$-pNE microcrystals. a) Schematic of two reaction steps: Sonochemistry and polymerization of NE. b) Bright-field (top) and fluorescence (bottom) images of a pNE-coated $CsPbBr_3$ microcube (left) and microplate (right) in DMF immediately after coating. c) Core-shell particles in DMF under UV lamp. d) XPS spectra of microcrystals with and without pNE coating. e) Spatial elemental maps of a core-shell microparticle for the cesium L line, lead M line, bromine L line, nitrogen K line, carbon K line, and oxygen K line. Numbers are the measured stoichiometry ratio of the Cs, Pb, Br, N, C and O content. f) Measured PXRD patterns of microcrystals with and without pNE coating, in comparison to a simulation result for the orthorhombic structure of $CsPbBr_3$ (space group Pbnm, a = 8.20 Å, b = 8.24 Å, c = 11.74 Å). g) Absorption spectra of uncoated and pNE-coated microparticles.

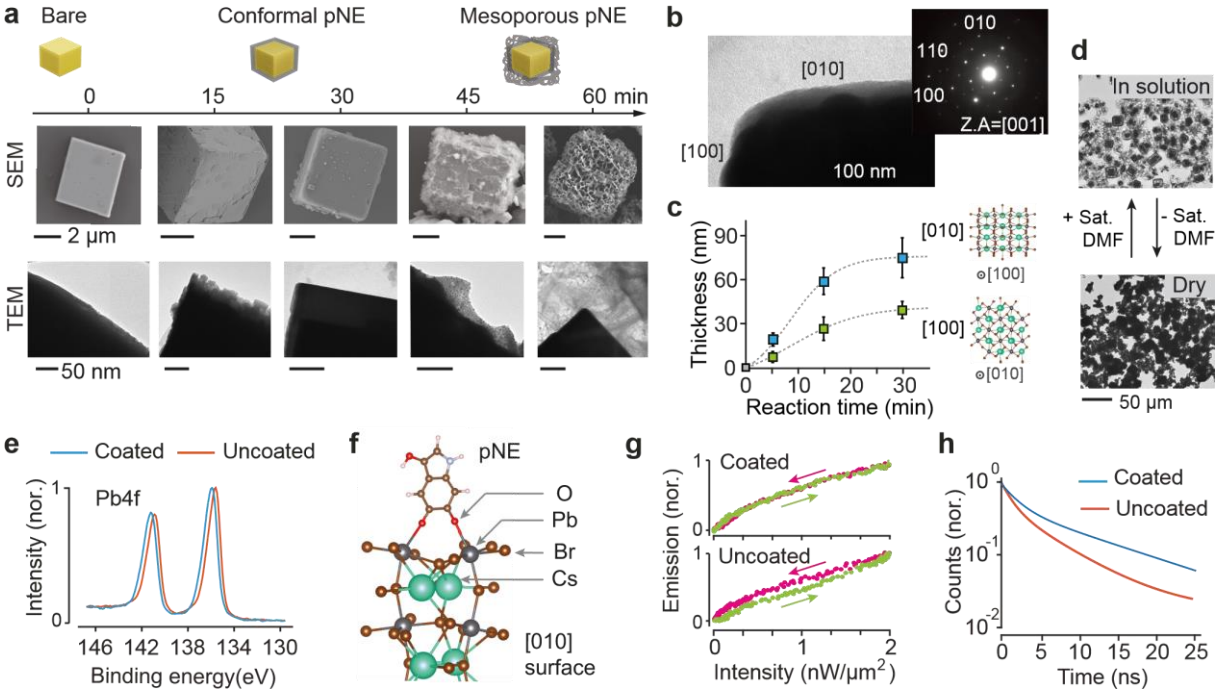

Figure 2. Structural and optical characterization. a) Time-lapse SEM and TEM images of different microparticles harvested at different reaction times, and schematic drawings of various reaction intermediates and final products. b) TEM image of the edge of conformal pNE coated $CsPbBr_3$. Corresponding selected area diffraction pattern in inset. c) Measured thickness of the thick and thin pNE layers at different reaction times. Dotted lines present sigmoidal fitting. Inset show the atomic structures of the two different planes. d) Optical transmission images of mesoporous pNE coated $CsPbBr_3$ with and without saturated DMF. e) High-resolution XPS of Pb4f in uncoated and pNE-coated samples. (f) DFT-optimized structure of pNE bound on under-coordinated Pb atoms on the (010) surface of $CsPbBr_3$. g) PL curves of bare and coated $CsPbBr_3$ microparticles upon continuous-wave excitation at 491 nm. h) PL decay of bare and coated microparticles upon picosecond excitation at 382 nm.

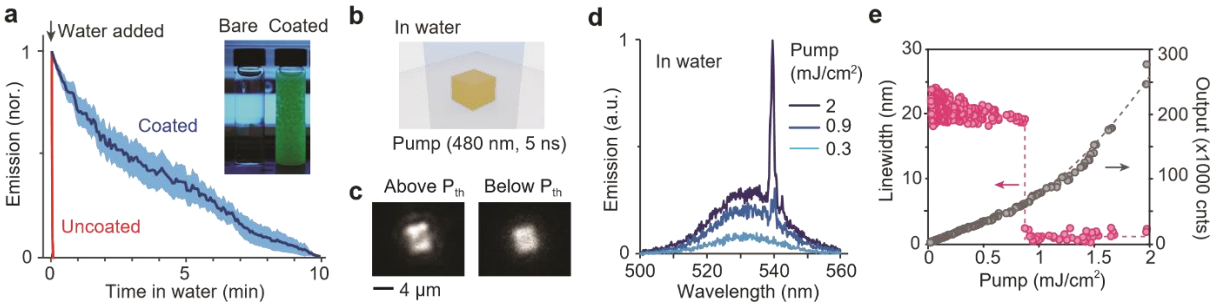

Figure 3. Lasing in water. a) Stability of bare and pNE-coated $CsPbBr_3$ microcrystals in water. The shaded region represents standard deviation of 15 different particles. b) Schematic of optical pumping. c) Emission spectra of a microparticle in water at two different pump fluences. d) Measured spectral linewidth and light-in-light-out curve of a laser particle in water at different pump fluences. A dramatic linewidth reduction occurs at the lasing threshold fluence of 0.85 mJ/cm^2. e) Emission intensity patterns below and above the threshold for a pNE-coated $CsPbBr_3$ microcrystal in water.

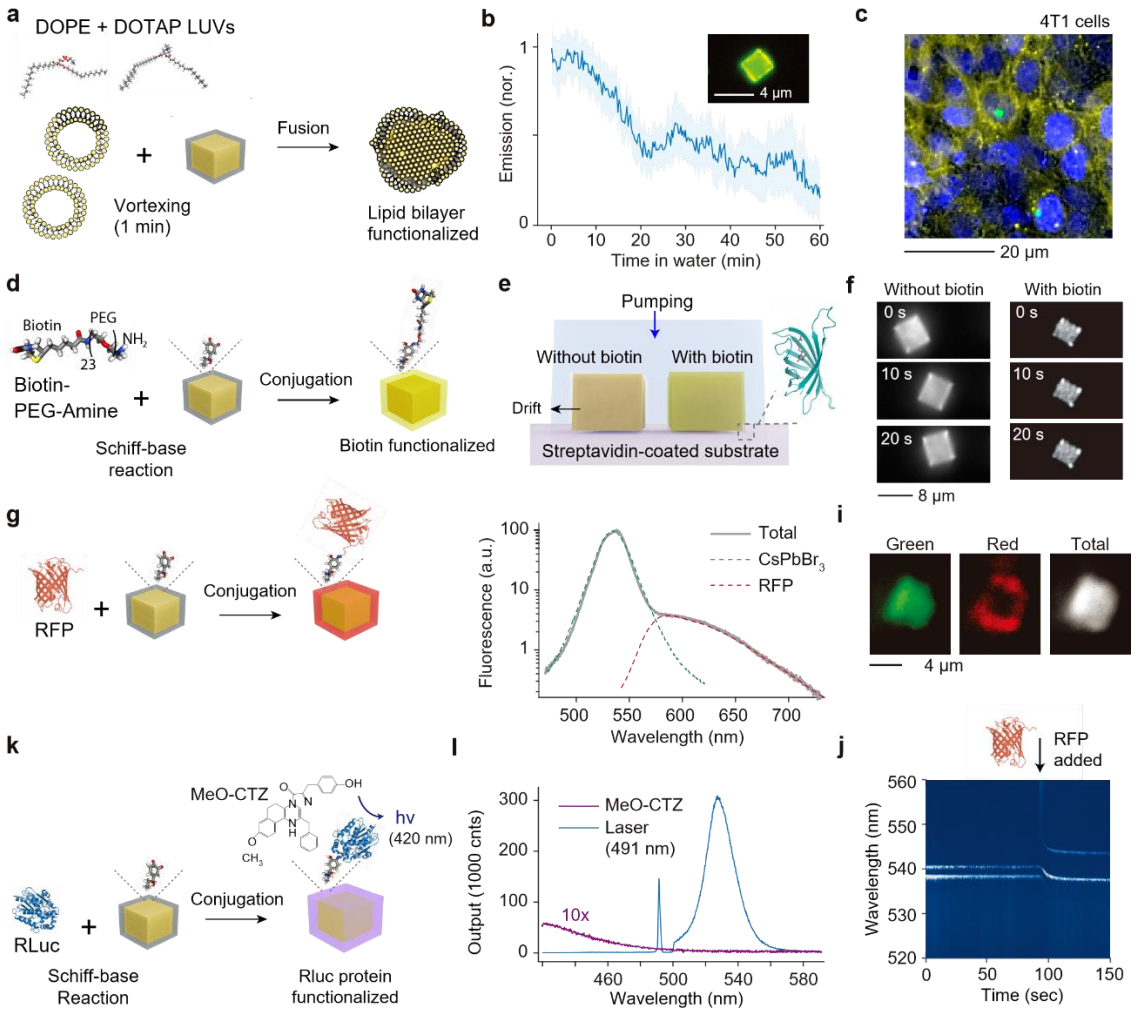

Figure 4. Biofunctionalization. a) Schematic of lipid-bilayer functionalization. b) Stability of lipid-coated microcrystals in water. The shaded region depicts the standard deviation of 15 different particles. Inset, image of a single microcube in water emitting green fluorescence from $CsPbBr_3$ and infrared fluorescence from DIR dye (rendered in yellow) conjugated to the lipid-bilayers. c) Fluorescence image showing the nuclei (DAPI, blue) of 4T1 tumor cells, lipid bilayers (DIR, yellow), and core-shell particles ($CsPbBr_3$, green). d) Schematic of biotinylation using biotin-$dPEG_{20}$-NH_2. e) Schematic of lasing experiment of bare and biotin-functionalized microparticles on the streptavidin coated substrate. f) Time-lapse images showing the immobilization of biotinylated particle due to biotin-streptavidin interaction. g) Schematic of RFP conjugation. h) Emission spectra from a $CsPbBr_3$-RFP conjugate particle. i) Fluorescence images of an RFP-coated particle. j) Time-lapse spectroscopy of 1.8 μm-sized laser particle in ethanol. The addition of RFP (10 μM) at 94 s causes a shift of the laser emission wavelength. k) Schematic of bioluminescence protein (RLuc) conjugation. l) Emission spectra from a single RLuc-coated particle. Purple curve: when mixed with MeO-CTZ (in PBS buffer), blue curve: under laser excitation at 491 nm at 1 $\mu W/\mu m^2$. The peak at 491 nm is due to residual pump light through a dichroic filter.